https://doi.org/10.1093/plphys/kiac028 PLANT PHYSIOLOGY 2022: 188: 2085–2100

Plant Physiology®

Research Article

Correlation of vacuole morphology with stomatal lineage development by whole-cell electron tomography

Wenhan Cao [1], Zhenping Li,[1] Shuxian Huang [1], Yuwei Shi,[1] Ying Zhu [1], Man Nga Lai [1], Pui Lok Lok [1], Xiangfeng Wang [2], Yong Cui[3] and Liwen Jiang [1,4,5,*,†]

1 School of Life Sciences, Centre for Cell & Developmental Biology and State Key Laboratory of Agrobiotechnology, The Chinese University of Hong Kong, Shatin, New Territories, Hong Kong, China
2 State Key Laboratory of Plant Physiology and Biochemistry, College of Biological Sciences, China Agricultural University, Beijing 100193, China
3 State Key Laboratory of Cellular Stress Biology, School of Life Sciences, Xiamen University, Xiamen 361102, China
4 The Chinese University of Hong Kong Shenzhen Research Institute, Shenzhen 518057, China
5 Institute of Plant Molecular Biology and Agricultural Biotechnology, The Chinese University of Hong Kong, Shatin, Hong Kong, China

*Author for correspondence: ljiang@cuhk.edu.hk
†Senior author.

W.C. and L.J. conceived and designed the experiments. W.C. performed the electron tomography analyses. W.C., Z.L., S.H., Y.S., Y.Z., M.N.L., and P.L.L. generated the 3D models. W.C., S.H., X.W., and Y.C. performed the other experiments. W.C. analyzed the data. W.C. and L.J. wrote the paper.
The author responsible for distribution of materials integral to the findings presented in this article in accordance with the policy described in the Instructions for Authors (https://academic.oup.com/plphys/pages/general-instructions) is: Liwen Jiang (ljiang@cuhk.edu.hk)

Abstract

Stomatal movement is essential for plants to optimize transpiration and therefore photosynthesis. Rapid changes in the stomatal aperture are accompanied by adjustment of vacuole volume and morphology in guard cells (GCs). In Arabidopsis (*Arabidopsis thaliana*) leaf epidermis, stomatal development undergoes a cell-fate transition including four stomatal lineage cells: meristemoid, guard mother cell, young GC, and GC. Little is known about the mechanism underlying vacuole dynamics and vacuole formation during stomatal development. Here, we utilized whole-cell electron tomography (ET) analysis to elucidate vacuole morphology, formation, and development in different stages of stomatal lineage cells at nanometer resolution. The whole-cell ET models demonstrated that large vacuoles were generated from small vacuole stepwise fusion/maturation along stomatal development stages. Further ET analyses verified the existence of swollen intraluminal vesicles inside distinct vacuoles at certain developmental stages of stomatal lineage cells, implying a role of multivesicular body fusion in stomatal vacuole formation. Collectively, our findings demonstrate a mechanism mediating vacuole formation in Arabidopsis stomatal development and may shed light on the role of vacuoles in stomatal movement.

Introduction

Stomata are a type of microscopic pore on the aerial surface of most land plants. Besides water vapor release and carbon dioxide uptake (Schroeder et al., 2001; Mustilli et al., 2002), stomata also serve as the gate for pathogen entry (Gudesblat et al., 2009). Stomatal development is strictly regulated by endogenous biochemical signals and environmental cues (Hetherington and Woodward, 2003). The epidermis of mature Arabidopsis (*Arabidopsis thaliana*) leaves mainly

Received November 01, 2021. Accepted December 22, 2021. Advance access publication February 2, 2022

derives from the differentiation of protodermal cells (Larkin et al., 1996, 1997). Prior to forming a mature stoma, a protodermal cell needs to undergo a series of intermediary divisions and transitions, known as the stomatal lineage (Bergmann and Sack, 2007). The lineage starts with a transition of the protodermal cell to the pluripotent meristemoid mother cell (MMC), followed by an asymmetric division producing two different daughter cells: the larger one is called the stomatal lineage ground cell (SLGC) and the other is the meristemoid. The meristemoid can either proceed by amplifying divisions to form more SLGCs, or transform into a guard mother cell (GMC; Larkin et al., 1997; Geisler et al., 2000). The transition from meristemoid to GMC is a morphological change involving an increase in size and a rounding-up of the cell. For subsequent differentiation, the GMC divides symmetrically, producing a couple of young guard cells (YGCs). Each YGC will further mature and expand into a mature guard cell (GC). Summarily, after division from MMC, the intact stomatal unit undergoes four stages: meristemoid, GMC, YGC, and GC (Pillitteri and Torii, 2012).

Because stomata mediate gas exchange and provide defense against pathogen invasion, stomatal movement is tightly controlled by the stomatal aperture (Munemasa et al., 2015). The mechanism underlying stomatal movement has been studied for decades (Scarth, 1927; Kim and Lee, 2007). Different environmental stimuli are sensed by receptors localized on the plasma membrane (PM), which triggers the downstream signaling pathways and results in changes of turgor pressure. Such stomatal movement is achieved via regulating turgor pressure and cell volume by water and ion channels (Pandey et al., 2007). Several molecular signaling pathways have been revealed in stomatal movement regulation, such as blue light, abscisic acid, and Ca^{2+} (Kim et al., 2010; Munemasa et al., 2015; Inoue and Kinoshita, 2017; Huang et al., 2019; Hosotani et al., 2021; Hsu et al., 2021).

Regarding their functions, plant cell vacuoles are classified into two types: protein storage vacuoles in seeds and lytic vacuoles in vegetative tissues (Paris et al., 1996). The lytic vacuoles are the largest organelles in plant cells (Shimada et al., 2018). Similar to lysosomes in animal cells and vacuoles in yeast cells, lytic vacuoles serve as a catabolic and digestive compartment (Marty, 1999). In regulating the signaling pathways in stomatal movement, vacuoles provide anchor sites for various ion channels and transporters (Pandey et al., 2007; Meyer et al., 2011; Andrés et al., 2014). Furthermore, vacuolar volumes have been shown to be tightly related with cellular volume changes during stomatal movement (Fricker, 1990; Andrés et al., 2014). A study on fava bean (*Vicia faba*) proved that the dynamics of the vacuolar membrane system might be essential for the rapid increase of vacuole volume in GCs (Gao et al., 2005). Since the appearance and disappearance of these vacuolar membrane structures are tightly related to stomatal movement, they were thought to serve as tonoplast reservoirs supporting the rapid changes on vacuole volume in *V. faba*. Another study in transgenic Arabidopsis expressing GFP–*At*VAM3 (green fluorescent protein-vacuolar morphology 3) also identified similar changes in vacuolar pattern (Tanaka et al., 2007). In addition to the vacuolar structures mentioned above, vacuolar convolution was shown to be essential for stomatal movement, which is coordinated with vacuolar acidification during stomata closing (Bak et al., 2013). Such vacuolar dynamics might be regulated via remodeling of actin filaments (Gao et al., 2009). Due to the limitation of 2D microscopy in describing intact vacuoles, several 3D reconstruction studies were performed based on a series of confocal images (Gao et al., 2005; Meckel et al., 2007; Tanaka et al., 2007; Andrés et al., 2014). In this way, vacuolar continuity was identified inside the GCs, which was further confirmed by a photobleaching analysis (Gao et al., 2005; Tanaka et al., 2007). However, given the complexity of vacuolar structures, 3D electron tomography (ET) analysis should be more suitable to investigate the spatial configurations. Based on their size in 3D, vacuoles were recently classified into small vacuoles, medium vacuoles, and large vacuoles in Arabidopsis root cortex cells (Cui et al., 2019). In this study, by performing 3D whole-cell ET analysis in stomatal lineage cells, we aim to answer the following questions: (1) what are the vacuole formation and development processes in stomatal lineage cells? and (2) do vacuole fission and fusion occur during stomatal movement?

Here, we first generated transgenic Arabidopsis lines stably expressing the tonoplast marker YFP-VAMP711 (yellow fluorescent protein-vesicle-associated membrane protein 711; Geldner et al., 2009) and the vacuolar lumen marker Aleu-Kaede, followed by examination of their subcellular localization and distribution in the four stages of stomatal lineage cells respectively via confocal laser scanning microscopy (CLSM). Subsequent whole-cell ET analyses were performed and the corresponding 3D models of vacuoles were built for the four stages of stomatal development. ET models of vacuoles and quantification analyses implied that the big central vacuoles of mature GCs were derived from the fusion and morphological transition of small vacuoles in earlier stages of stomatal development. ET analysis of vacuole inner space illustrated the existence of swollen intraluminal vesicles (ILVs) mainly in the large vacuoles of meristemoid and most vacuoles of GMC, indicating the involvement of multivesicular bodies (MVBs) fusion in the large vacuole formation of the stomatal lineage cells. Further photoconversion assay showed the co-existence of separate and interconnected vacuoles in GCs. In conclusion, our study establishes whole-cell ET models for vacuole morphology, development, and formation during stomatal development in plants, providing insights for future studies of vacuole function in GC volume changes during stomatal movement.

Results

Visualization of vacuole development in stomatal lineage cells

Several studies have proven that stomatal movement, accompanied by rapid changes in cell and vacuole volumes, is

related to vacuolar morphology and dynamics (Shope et al., 2003; Gao et al., 2005; Meckel et al., 2007; Andrés et al., 2014). In order to visualize vacuole morphology and dynamics in GCs, previous studies have used various fluorescence dyes to label the vacuolar lumen or vacuole-like vesicles, such as acridine orange (AO), LysoTracker Red DND-99 (an acidic organelle-selective cell-permeable probe; Gao et al., 2005), and 2,7-bis-(2-carboxyethyl)-5-(and-6)-carboxyfluorescein acetoxymethyl ester (BCECF-AM; Matsuoka et al., 1997; Andrés et al., 2014). In addition, multiple transgenic Arabidopsis lines expressing GFP-tagged tonoplast-localized membrane proteins have been developed, including the Soluble *N*-ethylmaleimide-sensitive Factor Attachment Protein Receptor (SNARE) family proteins, like the vacuolar Syntaxin-related protein *At*VAM3 (Uemura et al., 2002), and VAMP711 (Geldner et al., 2009). Additionally, propidium iodide (PI) is a kind of universal vital dye used in plants to stain the cell wall. Here, we used PI staining to distinguish cell boundaries in leaf epidermis.

To study the morphology and formation of vacuoles in plants, we have generated and utilized two distinct transgenic Arabidopsis marker lines: the tonoplast-localized YFP-VAMP711 and the vacuolar lumen marker Aleu-Kaede, which was tagged with a green-to-red photoconvertible fluorescent protein Kaede (Cui et al., 2019; Supplemental Figure S1A). As shown in Supplemental Figure S1B, in leaf epidermal cells of transgenic Arabidopsis plants expressing YFP-VAMP711, the YFP signals were found in the tonoplasts of both pavement cells (as indicated by closed arrows as examples) and stomata (as indicated by open arrows as examples), indicating the proper tonoplast localization of YFP-VAMP711. Similarly, in leaf epidermal cells of transgenic Arabidopsis plants expressing Aleu-Kaede, the GFP signals were found largely in the vacuolar lumen of mature GCs (as indicated by arrowheads as examples in Supplemental Figure S1C). Taken together, these markers are properly expressed and localized in their respective compartments in leaf epidermal cells of transgenic Arabidopsis plants.

The cell-fate transition of the stomatal lineage has been previously resolved in Arabidopsis (Pillitteri et al., 2007, 2011; Dong et al., 2009). Since only the meristemoid acquires the ability to develop into GCs, we mainly focused on the route from meristemoid to GCs in our study. To have an overview of vacuole patterns in the stomatal development process, we next studied the subcellular localization of these two marker proteins in Arabidopsis stomatal lineage cells. As shown in Figure 1A and Supplemental Figure S2A, the lineage is initiated with meristemoid. Before differentiating into an oval-shape, the GMC undergoes an angular stage. Through a symmetric division, it transforms into the functional stomatal unit. YFP-VAMP711 was first used to study vacuole morphology and distribution in stomatal lineage cells, including GCs from closed and open stomata (Supplemental Figure S2B). As illustrated by both tonoplast (YFP-VAMP711) and vacuolar lumen markers (Aleu-Kaede), vacuoles occupy most of the internal space in lineage cells during the whole developmental stage (Figure 1, B and C).

Whole-cell ET analyses of vacuole distribution and formation in stomatal lineage cells

To investigate vacuoles in GCs, previous research has mainly relied on CLSM with a limitation of 200-nm resolution (Gao et al., 2005; Bak et al., 2013) and 2D transmission electron microscopy with a limitation in resolving the spatial relationship and complexity of vacuolar inner structures (Brown and Lemmon, 1985; Zhao and Sack, 1999; Gao et al., 2005; Andrés et al., 2014). Therefore, observations of vacuole morphology and membrane at the nanometer level are better obtained by ET approach (Weiner et al., 2021).

We performed high-pressure freezing/freeze substitution and whole-cell ET analysis on meristemoid, GMC, YGC, and

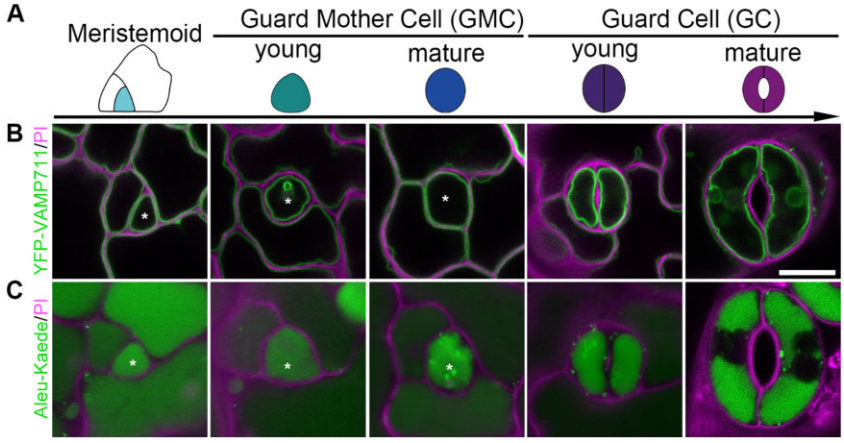

Figure 1 Vacuole development and distribution in stomatal lineage cells of Arabidopsis cotyledon epidermis. A, Schematic diagram showing color-coded models of stomatal lineage cells in five developmental stages: Meristemoid, cyan; young GMC, green; mature guard mother cell, blue; YGC, indigo; and mature GC, purple. B and C, Dynamics and subcellular localization of the two distinct organelle markers in the five corresponding stages of stomatal lineage cells, including the tonoplast marker YFP-VAMP711 (B), and the vacuolar lumen marker Aleu-Kaede (C). Asterisks indicate the corresponding lineage cells in each stage. Cell walls stained with PI (magenta). Scale bar, 10 μm for all panels.

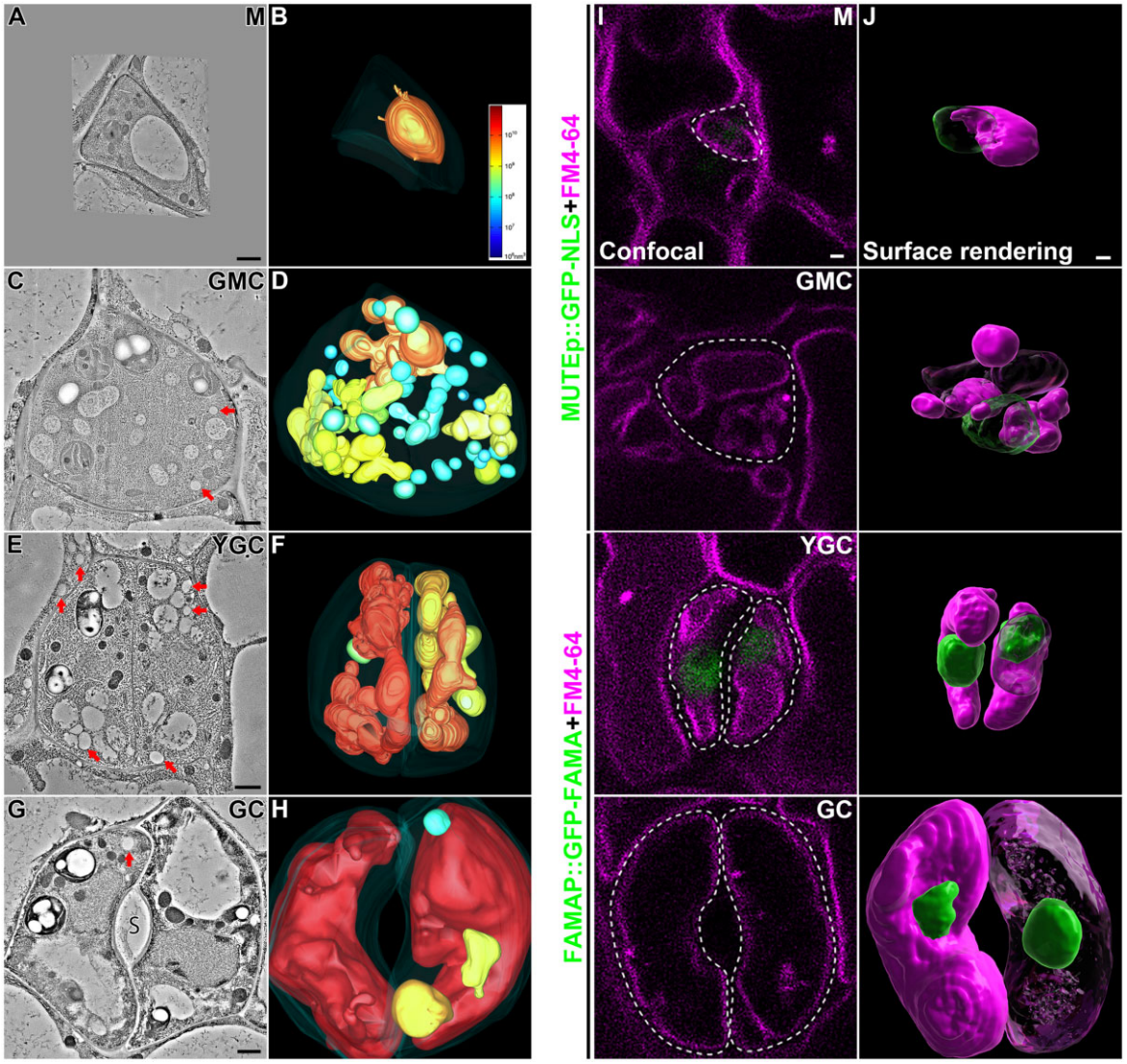

Figure 2 Whole-cell ET analyses and surface renderings of vacuoles in stomatal lineage cells of Arabidopsis cotyledon epidermis. A–H, Representative tomographic slices generated from 250-nm-thick sections of four stomatal lineage cells, M (meristemoid), GMC, YGC, and opening mature GC are shown in (A), (C), (E), and (G), respectively. Their corresponding 3D whole-cell vacuole models (B, D, F, and H) were built and color-coded according to the vacuole volume. The color scale bar in (B) indicates the colors representing certain vacuole volume. The PM is shown in semi-transparent fashion. The arrows indicate examples of LDs. S, stoma. Scale bars, 1,000 nm. Also see Supplemental Movies S1–S4. I, J, Surface renderings of vacuoles and nuclei from stomatal lineage cells. Cotyledons from 3-d-old transgenic Arabidopsis plants expressing nucleus markers (MUTEp::GFP-NLS in meristemoid and GMC, and FAMAp::GFP-NLS in YGC and GC) were proceeded for overnight incubation of FM4–64 and subsequent constant washing in half-strength MS for 5 h in orbital shaker. Confocal images of stomatal lineage cells were taken, each of which was a stack of about 30 single images with 0.4-mm interval. Representative optical slices of each cell were shown, with green (GFP) and magenta (FM4–64) fluorescent channels (I). Cell boundaries are displayed in dash lines. Note that no visible nuclear signal was observed on the focal planes of M, GMC, and GC. Z-stack images were proceeded to Imaris software for surface renderings of vacuoles (magenta) and nuclei (green) (J). Note that parts of nuclei and vacuoles were transparentized. Scale bars, 1,000 nm for all panels.

GC from 3-d post germination (dpg) abaxial cotyledons (Figure 2). For each stage, four candidates were picked and one of them was chosen for subsequent ET analysis (Supplemental Figure S3). Whole-cell ET and corresponding vacuole models were generated from around 40 serial sections (each with ~250-nm thickness) for each cell. For each of the other candidates, four serial sections were also cut to generate ET models (Supplemental Figure S4). 3dmod program was used to calculate the exact volume of each intact vacuole.

Based on the ET models, we first calculated the vacuole number and size. Meristemoid contained one single large vacuole (Supplemental Figure S4A and Supplemental Table S1). Interestingly, when the meristemoid was converted to GMC, the number of small vacuoles increased to 29 along with the formation of 11 medium vacuoles and one visible large vacuole, where large vacuoles, medium vacuoles, and small vacuoles took up 29%, 50%, and 21% of the combined vacuole volume, respectively (Supplemental Table S1). After completing the symmetric division, the number of small

vacuoles dramatically decreased to two along with two medium vacuoles and three large vacuoles, where large vacuoles, medium vacuoles, and small vacuoles took up 91%, 7%, and 2% of the combined vacuole volume, respectively (Supplemental Table S1). After maturation to GC, three large vacuoles, one medium vacuole, and one small vacuole were finally identified, where large vacuoles, medium vacuoles, and small vacuoles took up 99.1%, 0.8%, 0.1% of the combined vacuole volume (Supplemental Table S1).

The morphology of vacuoles identified in these four cells also varied. The large vacuole showed an ellipsoid-like shape in the meristemoid (Figure 2, A and B; Supplemental Figure S4A and Supplemental Movie S1). In GMC, the large vacuole and medium vacuoles exhibited a much more complicated shape, whereas the small vacuoles acquired a much bigger proportion than that of the other three cells (Figure 2, C and D; Supplemental Figure S4B and Supplemental Movie S2). Additionally, the large vacuoles were more convoluted in YGC, indicating that vacuoles were undergoing expansion or compression during this stage (Figure 2, E and F; Supplemental Figure S4C and Supplemental Movie S3). Since membrane fusion consumes a substantial amount of energy, it may be economical for a plant cell to achieve multiple fusions of membranous organelles simultaneously (Jahn et al., 2003). Therefore, such a grape-like morphology of the vacuoles implied that they were undergoing multiple fusion events to form large vacuoles and such convoluted morphology could be an intermediate state prior to maturation. The open stoma was surrounded by a pair of GCs, each one containing a single big central vacuole (Figure 2, G and H; Supplemental Figure S4D and Supplemental Movie S4). Intriguingly, in addition to the central vacuoles, the isolated medium vacuole and small vacuole were identified in one of the GCs, confirming that different vacuolar compartments are separate in plant cells. Considering that the cell size of the GCs would further increase, the big central vacuoles would require more nascent small vacuoles and medium vacuoles as membrane sources. In addition to the open stoma, we also performed ET analysis on three closed stomata from 3-dpg abaxial cotyledons (Supplemental Figure S5 and Supplemental Movie S5). For each pair of GCs, 9 to 10 consecutive sections (each with about 250-nm thickness) were collected for ET and 3D reconstruction (Supplemental Figure S5, A, C and E). Although large vacuoles took the major part of the cellular volume in both GCs, the numbers of medium vacuoles and small vacuoles were higher than that of open stomata. Two models of tonoplast invaginations were also constructed: both models (Supplemental Figure S5, B and D) suggested that the large vacuoles in GCs might be separated to generate smaller vacuoles through membrane fission during the transition from stomata opening to closing. The isolated large vacuoles in Supplemental Figure S5F might be due to such a vacuolar fission.

Further statistical analyses revealed that the average volume of vacuoles increased while the number of small vacuoles dramatically decreased from GMC to GC (Supplemental Table S1), implying that newly generated small vacuoles fused together in the late stage of stomatal lineage cells. Meanwhile, the combined vacuole volume and vacuolar occupancy increased as cell size grew, suggesting a putative role of vacuole in cell expansion. However, the combined vacuole volume of GC (2.31×10^{11} nm^3) was more than 5-fold of that in YGC (4.02×10^{10} nm^3), while the vacuolar occupancy of GC was only about triple of that in YGC, implying that nascent vacuoles had received more membrane than PM did during YGC transforming to GC. Nevertheless, YGC acquired the highest vacuolar surface area among these four cells. Taken together, the whole-cell ET analyses gave us an overview on vacuole formation along with stomatal development from meristemoid to GC: in the meristemoid, there is only one central large vacuole; in the GMC, more small vacuoles and medium vacuoles are generated and the large vacuole gets enlarged potentially via fusion with small vacuoles and/or medium vacuoles; in the YGC, vacuoles are converted into a convoluted morphology, preparing for subsequent central vacuole enlargement; eventually in GC, one single central vacuole occupies most of the cellular space with less medium vacuoles and small vacuoles.

Distinct from the 2D confocal images (Figure 1, B and C), the whole-cell ET models showed that vacuoles took up $<50\%$ of the inner cellular space in stomatal lineage cells. Given these discrepancies, we wondered how the fluorescence-labeled vacuoles would look like in 3D projections. Since the nucleus is considered a big organelle in the early developmental stage (Zhao and Sack, 1999), we also included nucleus markers to illustrate the spatial relationship between nucleus and vacuoles. Thus, 3D reconstruction analysis was performed on Z-stack images of FM4–64 stained vacuoles in stomatal lineage cells expressing the nuclear markers (Meristemoid and GMC in MUTEp::GFP-NLS, YGC and GC in FAMAp::GFP-FAMA; Adrian et al., 2015). The single optical section of confocal images showed that the nuclei were not on the focal plane of the big central vacuoles (Figure 2I). Intriguingly, surface rendering revealed similar vacuole distribution in meristemoid and GC compared to the corresponding ET models, but vacuole distribution determined by surface rendering was distinct from the models in GMC and YGC (Figure 2J). The vacuole number shown by surface rendering was 7 in total, which was less than that of ET (41) in GMC. Moreover, the vacuole morphology displayed by surface rendering was simpler and smoother than that of the ET model in YGC. Nevertheless, both the 3D confocal and ET approaches showed a similar vacuole development process from meristemoid to GC, in which it started with a pre-existing large vacuole in meristemoid, followed by de novo formation of small vacuoles and medium vacuoles in GMC and YGC, and ended with the formation of big central vacuoles in GC.

Fusion of small vacuoles containing ILVs leads to the formation of large vacuoles prior to the symmetric division of GMC

A recent study demonstrated that the generation of small vacuoles via homotypic fusion among MVBs is essential for vacuole biogenesis in root cortex cells and that the maturation of the vacuoles is accompanied by a gradual degradation of ILVs (Cui et al., 2019). To understand the possible roles of small vacuoles in the formation of the central vacuoles in stomatal lineage cells, we also examined the inner details of vacuolar lumen (Figure 3) in these cells via zoom-in ET analyses and model building. Intriguingly, swollen ILVs were identified in the large vacuole of meristemoid (Figure 3, B and C, arrowheads) and GMC (Figure 3, E and F, arrowheads), but were hardly present in vacuoles of YGC (Figure 3, H and I), albeit a single one presented in the large vacuole of GC (Figure 3, K and L, arrowheads). Additionally, the sole large vacuole seemed to be undergoing fusion with small vacuoles/medium vacuoles in GMC (Figure 3, E and F, closed arrows). These results are consistent with a previous observation where vacuole maturation was accompanied by the gradually degradation of ILVs during the late stages of root cell development (Cui et al., 2019). The sporadic observation of ILVs in GC might indicate that continuous large vacuole formation is required for the further development of the central vacuoles. On the cotyledon epidermis prepared for ET analysis, we also identified a symmetrically dividing GMC, which lay on the developmental route from GMC to YGC. Although the cytoplasm was still connected between two daughter cells during cytokinesis, the vacuoles were already separated by cell plate/cell wall (Supplemental Figure S6, A and B and Supplemental Movie S6). Further zoom-in view on the square-box region ($z = 720$) revealed a jigsaw puzzle pattern formed by adjacent tonoplasts (Supplemental Figure S6, C and D, $z = 684$, $z = 710$). The close association of two vacuoles with cell wall may imply that these two vacuoles resulted from the fission of one larger vacuole in GMC and, subsequently, separated by the nascent cell wall during cytokinesis. Taken together, these ET analyses suggest that small vacuoles and medium vacuoles start to substantially accumulate in GMC before symmetrical division and would finally form large vacuoles preparing for cytokinesis.

To investigate the possible role of ILVs in vacuole formation, we extended the ET analysis on ILVs in the vacuoles of the GMC and color-coded the 3D models as follows: (1) vacuoles with ILVs (red); (2) vacuoles without ILVs (cyan); and (3) ILVs (white; Figure 4A; Supplemental Movie S7). Most of the ILVs (Figure 4, B and C, arrowheads), which were present in the vacuolar lumen of the GMC, acquired a bigger diameter than that in regular MVBs (30–40 nm, Figure 4F; (Shen et al., 2018), which may be due to the osmotic pressure difference between MVBs and vacuoles. Most of the vacuoles containing ILVs were medium vacuoles, likely formed or forming from the fusions of small vacuoles with ILVs (Figure 4, B and C, the closed arrow), whereas all the vacuoles without ILVs were separated small vacuoles (Figure 4, D and E).

Previous ET analyses have already shown the presence of single ILVs in the MVB lumen of yeast (Adell et al., 2014), mammalian cells (Murk et al., 2003), and plant cells (Otegui et al., 2006), suggesting that ILVs may bud off independently from the limiting endosomal membrane. However, recent studies also suggested the occurrence of ILV concatenation in MVB as an alternative mechanism of vesicle formation in plant cells (Buono et al., 2017; Liu et al., 2021a). However, it remains elusive how the concatenated ILVs split into isolated ILVs in plant cells. In this study, we also obtained an ET model of MVB from the cotyledon epidermal cell, which showed similar networks of concatenated ILVs (Figure 4, F and G; Supplemental Movie S8). Zoom-in views further showed that two adjacent ILVs were interconnected by a narrow membrane bridge (Figure 4, H and H′), which was similar to that in root cells (Buono et al., 2017). Intriguingly, in the vacuolar lumen of GMC, we found an ILV with invagination on the membrane surface (Figure 4I). This dumbbell-like ILV may imply that swollen ILVs are derived from the membrane bridge swelling between two concatenated ILV spheres.

To unravel the possible correlation between ILVs and vacuoles, we subsequently performed statistical analysis and showed that the average volume of vacuoles with ILVs (8.22×10^8 nm^3) was much higher than that of vacuoles without ILV (1.61×10^8 nm^3; Figure 4J). Meanwhile, vacuoles with ILVs (94.06%) dominated the combined vacuole volume of the GMC as compared to vacuoles without ILV (5.94%; Figure 4J). Moreover, the higher vacuolar volume/surface ratio of vacuoles with ILVs (120.85 against 106.21 of vacuoles without ILV) further supports the assumption that these vacuoles are derived from fusions of small vacuoles containing ILVs (Figure 4J). Such swollen ILVs would be gradually degraded (Cui et al., 2019) and the debris left in vacuoles making them easy to be distinguished from lipid droplets (LDs, indicated by open arrows in Figure 4C). Further analysis revealed that the average volume of ILVs within vacuoles (9.66×10^5 nm^3, 7.91×10^5 nm^3, and 1.04×10^6 nm^3 for that of small vacuole, medium vacuole, and large vacuole, respectively) reached around 30 folds of single ILVs in MVBs (3.16×10^4 nm^3; Figure 4K). The quantification analysis of average volume/surface ratio suggested that the morphology of swollen ILVs made no difference in distinct types of vacuoles (18.82, 18.29, and 19.34 for that of small vacuole, medium vacuole, and large vacuole, respectively; Figure 4K). Taken together, these results demonstrate that fusions of small vacuoles containing ILVs facilitate the formation of medium vacuoles and subsequent transition to large vacuoles, a conclusion mainly based on 3D whole-cell ET analysis of GMC during stomatal development.

Vacuoles in mature GCs of the same stomatal pair

As shown in Supplemental Figure S7, open stomata contain large central vacuoles and the large vacuoles undergo

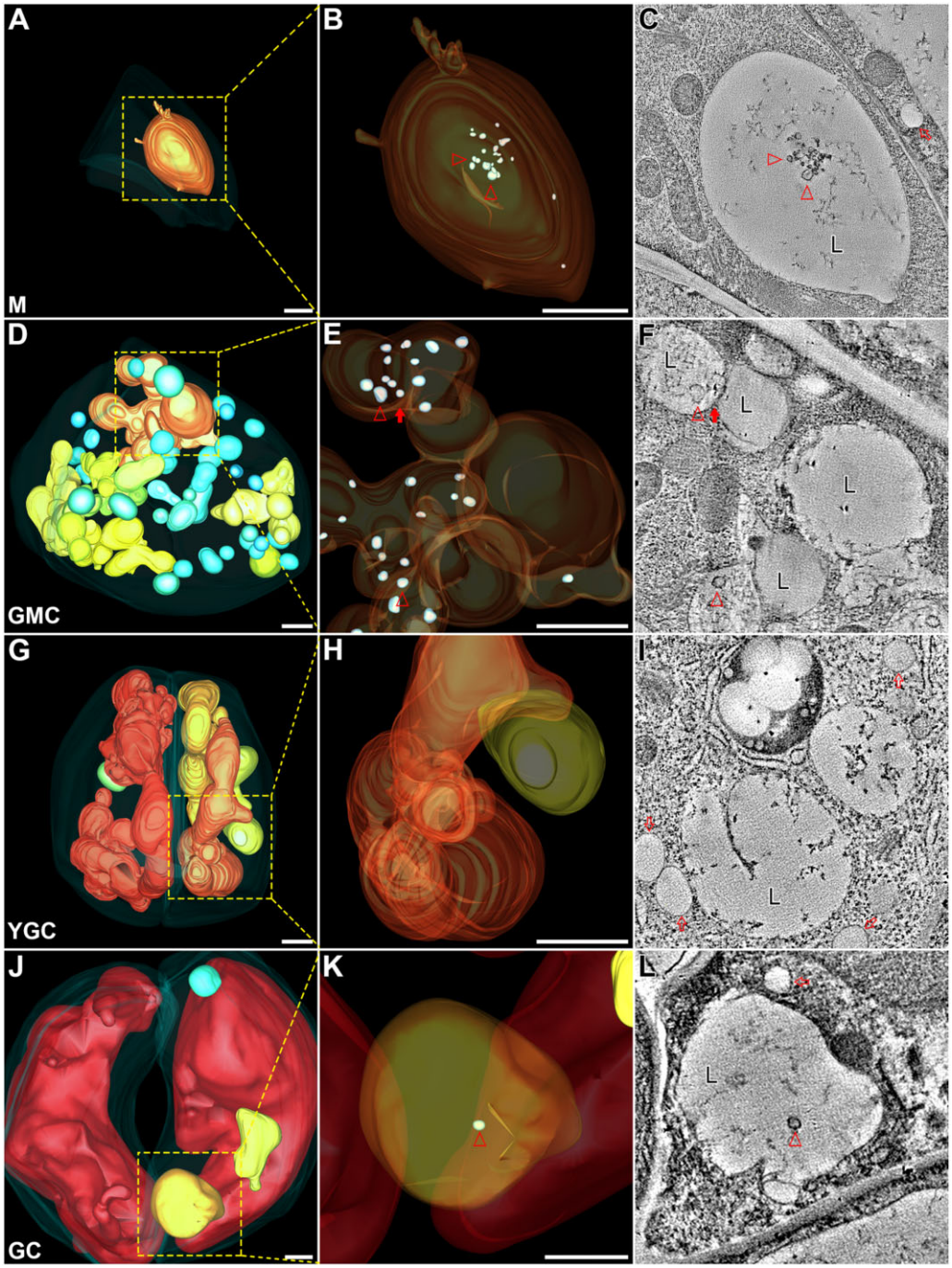

Figure 3 Swollen ILVs are present in the large vacuoles of the stomatal lineage cells. The indicated square boxes in each whole-cell ET model of M (A), GMC (D), YGC (G), GC (J) were further zoomed-in for ET analysis with their corresponding enlarged models shown in (B), (E), (H), (K), respectively. Their representative tomographic slices were shown in (C), (F), (I), (L), respectively. Semi-transparent models of large vacuoles display internal details. Small vacuoles were omitted in GMC to avoid unexpected block (E). Arrowheads indicate examples of swollen ILVs in 3D ET models (B, E, and K) and their corresponding tomographic slices (C, F, and L). Note that multiple large vacuoles in GMC are interconnected (E and F). The closed arrow indicates a direct membrane connection between the two large vacuoles (F). The open arrows indicate examples of the lipid droplets (I). M, meristemoid; L, large vacuole. Scale bars, 1,000 nm for all the figure parts.

morphological changes that coincide with stomata closure (Gao et al., 2005). Previous studies have shown that distinct vacuolar compartments are interconnected via various vacuolar structures in the same GC, either open or closed (Gao et al., 2005; Tanaka et al., 2007). However, a recent study in Arabidopsis root cells expressing Aleu-Kaede demonstrated that vacuoles are mostly separated from each other (Cui et al., 2019). To gain insight into the physical relationship of

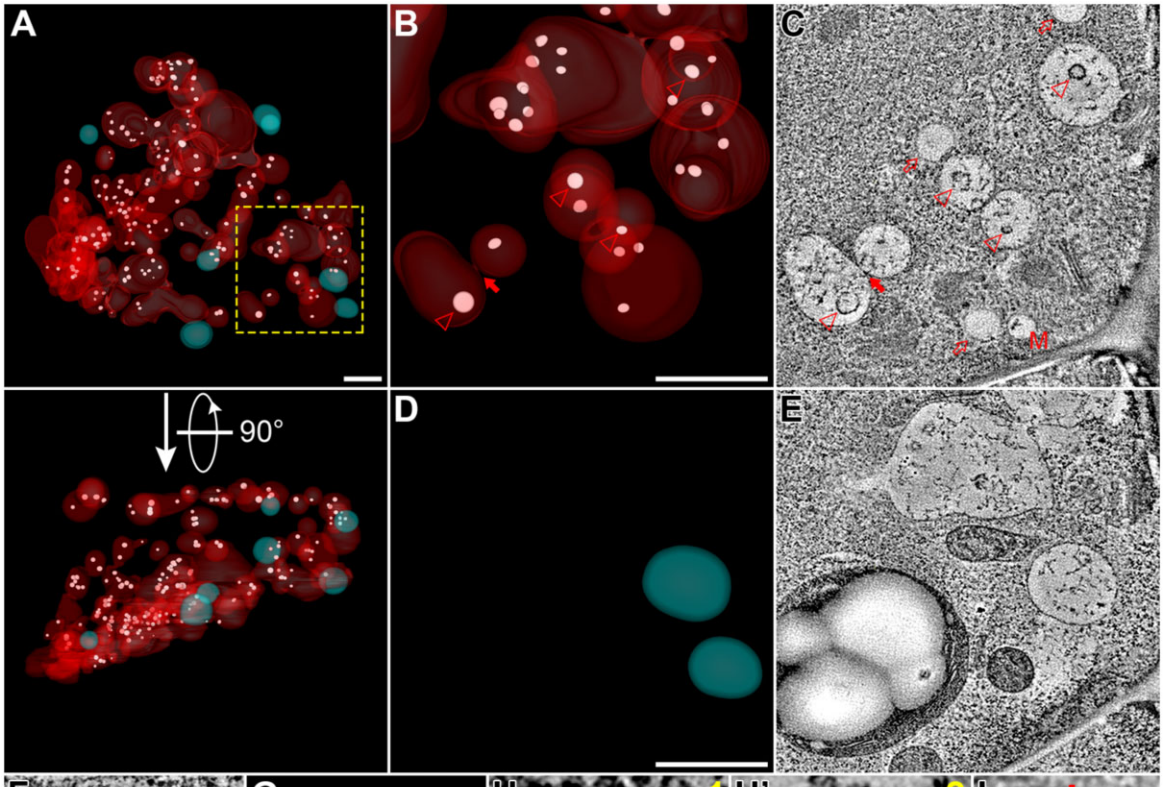

J

Sample[a]	i	ii
Average vacuolar volume/nm^3	8.22E+08	1.61E+08
Proportion in combined vacuole volume	94.06%	5.94%
Average ratio of vacuole volume/surface area	120.85	106.21

K

Sample[b]	MVB	SV	MV	LV
Average ILV volume/nm^3	3.16E+04	9.66E+05	7.91E+05	1.04E+06
Average ratio of ILV volume/surface area	N/A	18.82	18.29	19.34

[a] i: n=31 for vacuoles with ILVs; ii: n=10 for vacuoles without ILV.
[b] n=98 ILVs from 3 MVBs; n=110 (SV), 96 (MV), and 32 (LV).

Figure 4 Most vacuoles in GMC contain swollen ILVs. A, The whole-cell ET model of vacuoles and swollen ILVs in GMC. 3D models are color-coded: Vacuoles with ILVs (red), vacuoles without ILV (cyan), and ILVs (white). All 3D models are shown in semi-transparent fashion. A perpendicular view is shown in bottom part. Scale bar, 1,000 nm. Also see Supplemental Movie S7. B–E, The indicated square box in (A) was further zoomed-in for ET analysis with enlarged models shown in (B) and (D). Vacuoles without ILV were omitted in (B) and vacuoles with ILVs were omitted in (D). Their representative tomographic slices are shown in (C) and (E), respectively. Arrowheads indicate swollen ILVs in tomographic slice (C) and their corresponding 3D models (B). The closed arrow indicates a direct membrane connection between two vacuolar compartments with ILVs (B and C). Open arrows indicate lipid droplets (C). M, multivesicular body, MVB. Scale bars, 1,000 nm for all panels. F and G, Representative tomographic slice (F) and corresponding 3D model (G) of a MVB from WT Arabidopsis cotyledon epidermis. Single ILVs were colored in cyan and concatenated ILVs were colored in white. WT, wild-type. Scale bars, 100 nm. H and H′, The indicated square boxes in (G) were further zoomed-in, showing details of the concatenated ILV buds connected to the endosomal limiting membrane. Red arrows (upper) indicate membrane interconnections with corresponding 3D models (lower). Scale bars, 20 nm for all figure parts. I, Representative tomographic slice (upper) and corresponding 3D model (lower) of a swollen ILV in GMC. Red arrow indicates shallow invagination on the membrane surface. Scale bar, 20 nm. J, Quantification analyses on vacuolar parameters of the two types of vacuoles in GMC: i, vacuoles with ILVs and ii, vacuoles without ILV. N = 31 for vacuoles with ILVs, n = 10 for vacuoles without ILV. K, Quantification analyses on ILV parameters: n = 98 ILVs from 3 MVBs; n = 110 (SV), 96 (MV), and 32 (LV). SV, small vacuole; MV, medium vacuole; LV, large vacuole.

vacuolar lumen in the GCs and determine whether vacuoles are interconnected or not, we performed photoconversion assays in GCs of transgenic Arabidopsis Aleu-Kaede lines as before. In the GCs of an open stoma, the vacuolar lumen was labeled by Aleu-Kaede in green prior to photoconversion (Figure 5A). Upon first excitation by 405-nm UV light

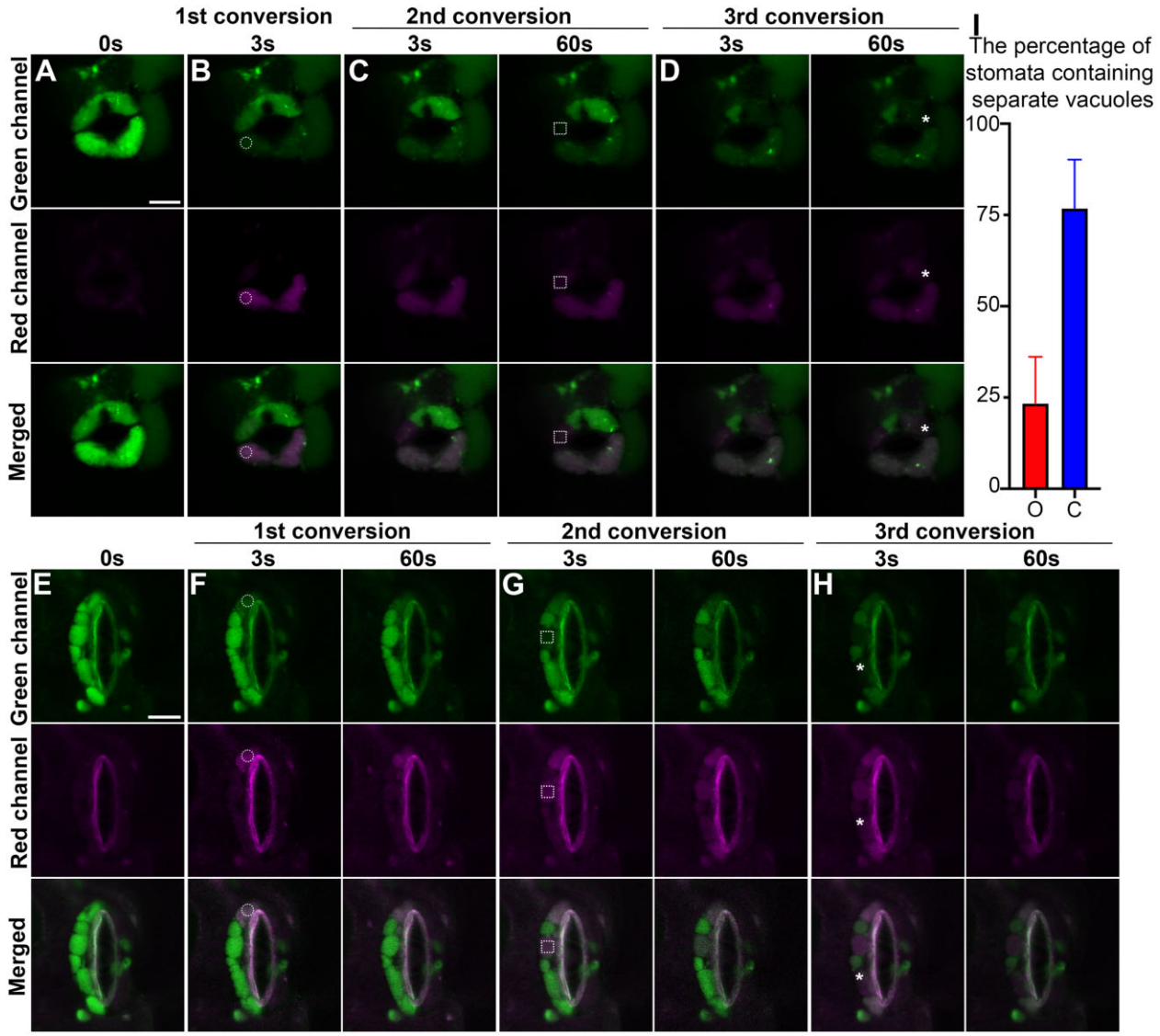

Figure 5 In vivo physical relationship of vacuoles in opening and closed stomata from Arabidopsis cotyledon epidermis. Opening and closed stomata from transgenic Arabidopsis plant, which expresses the photoconvertible vacuole-localized marker Aleu-Kaede, were subjected to photo-activation and conversion experiments sequentially at three time points as indicated, followed by confocal imaging at respective channels. The circles in (B and F), the square boxes in (C and G), and the asterisks in (D and H) indicate the positions of each photo-activation, respectively. The green channel (top) shows the original Aleu-Kaede signals whereas the Red channel (middle) exhibits the activated/converted signals after photo-activation. Scale bars, 10 μm for all figure parts. A and E, Control prior to photo-activation and conversion, showing the vacuoles with luminal green signals in the two GCs. B and F, Confocal imaging at 3 s (B and F) and 60s (F) post first conversion. The white circles indicate the regions of photo-activation. C and G, Confocal imaging at 3 s and 60 s post second conversion, respectively. The white square boxes indicate the regions of photo-activation. D and H, Confocal imaging at 3 s and 60 s post third conversion, respectively. The asterisks indicate the regions of photo-activation. I, Statistical analysis on the percentage of stomata containing separate vacuoles. O, opening stomata; C, closed stomata. Data are shown as mean ± SD of three repeats. $n = 20$.

in the lower GC as indicated by the circle in Figure 5B, the photoconverted Aleu-Kaede protein spread from the excitation site to the rest of the central vacuole within 3 s, illustrating a single central vacuole in this cell. In contrast, upon second excitation in the other GC surrounding the same stoma indicated by the square, the red signal of photoconverted Aleu-Kaede was restricted to a limited region (Figure 5C). After 60 s, which was sufficient to allow converted Aleu-Kaede molecules to disperse inside the interconnected vacuole, the red signal was restricted to the same region. A similar result was observed at the third conversion: upon activation, the photoconverted signal remained in the other side of upper GC, without diffusing even 60 s after conversion (indicated by the asterisk in Figure 5D). The photoconversion assay was also carried out in one GC of a closed stoma. Different red vacuolar compartments (photoconverted) were isolated by green ones (nonconverted) (Figure 5, E–H). Further statistical analysis

indicated that the interconnecting status of vacuoles closely relied on the stomatal movement (Figure 5I). Taken together, these results suggest that the lumens of different vacuoles are not always interconnected in the same pair of GCs, despite that vacuoles may form a continuum while the stoma is completely open.

Discussion

Vacuoles in root cells versus GCs

To maintain cellular homeostasis and to coordinate with environmental factors, vacuoles play indispensable roles in plant morphogenesis (Rojo et al., 2001), development (Seguí-Simarro and Staehelin, 2006; Olbrich et al., 2007), and cell elongation (Scheuring et al., 2016). Lack of functional vacuoles may result in severe defects in plant cells, such as embryonic lethality (Rojo et al., 2001; Gao et al., 2014) or development arrest (Cui et al., 2014). Therefore, plant vacuoles have unique features that are distinguished from yeast vacuoles and mammal lysosomes, which mainly serve as sites of protein degradation and material recycling (Cui et al., 2020). In this context, a classical model of vacuole biogenesis was raised, where vacuoles originated from endosome fusion/maturation (Marty, 1978, 1999). Previously, antibodies specific for different isoforms of the tonoplast intrinsic proteins (TIPs) were used as specific markers for different vacuoles, with α-TIP labeled protein storage vacuoles (PSVs) and γ-TIP labeled lytic vacuoles (Paris et al., 1996; Jauh et al., 1999). However, a subsequent study using transgenic Arabidopsis plants expressing different YFP fusions with α-, γ-, and δ-TIPs under the control of the 35S or native promoter failed to identify separate vacuolar compartments in various cell types, suggesting that the distribution of TIPs was tissue and development specific rather than organelle specific (Hunter et al., 2007). Interestingly, an ultrastructural study showed that during seed germination and vegetative tissue maturation, α-TIP was gradually replaced by γ-TIP on the vacuole membrane, thus suggesting that the lytic vacuoles were derived from the PSVs upon the mobilization of the storage molecules during seed germination (Zheng and Staehelin, 2011). Several recent studies suggested a new model where vacuoles are interconnected in plant cells. In these studies, multiple approaches have been utilized: (1) CLSM-based 3D reconstruction of BCECF-AM stained vacuoles in Arabidopsis root cells of wild-type (WT; Viotti et al., 2013) and *fyve1/free1* (Fab1, YOTB, Vac1, and EEA1 domain-containing protein 1/FYVE domain protein required for endosomal sorting 1) mutant (Kolb et al., 2015); (2) fluorescent recovery after photo-bleach (FRAP) assays evaluating the vacuolar lumen in the root epidermis (Scheuring et al., 2016); and (3) serial block-face scanning electron microscopy based 3D reconstruction (Scheuring et al., 2016). On the other hand, a vacuolar continuum model has also been raised in GCs based on 3D confocal imaging and FRAP assay (Gao et al., 2005; Tanaka et al., 2007; Andrés et al., 2014). Vacuolar compartments were considered to be linked by distinct intravacuolar membrane structures (Gao et al., 2005), which might serve as a reservoir of tonoplasts and maintain the integrity of the tonoplasts during stomatal movement.

A recent whole-cell ET analysis, in combination with photoconversion assay has demonstrated that many vacuoles were physically separate in Arabidopsis root cortical cells (Cui et al., 2019). During stomata switch between opening and closure, the vacuoles display dynamic changes in GCs (Andrés et al., 2014). In open stomata, the tonoplasts appear in large compartments occupying most of the GC volume (Supplemental Figure S7, A and B), whereas in closed stomata, the tonoplasts are partitioned into smaller compartments and invaginations (Supplemental Figure S7, C and D). This feature makes GC a good single-cell model to study possible vacuole fusion and fission during stomatal movement.

In this study, our results support a model with a unique feature of separate vacuoles (Figures 2 and 5). The existence of two distinct vacuole models may be due to: (1) the 200-nm resolution of CLSM might not be able to distinguish complex vacuolar structures and the closely associated vacuoles (Cui et al., 2019); (2) the fluorescent dyes, like AO or BCECF, might label other acidic compartments (e.g. MVB; Shen et al., 2013) besides vacuoles during high-resolution imaging; and (3) vacuoles might switch between interconnection and isolation depending on the stomatal movement because both conditions have been identified in the same pair of stomata (Figure 5). To further support our whole-cell ET analysis, three additional ET models were also generated for each stomatal lineage cell, respectively. Although each of these additional ET models was derived from four serial sections, they provided a glimpse into the inherent variability of vacuole morphology in stomatal lineage cells. As shown in Supplemental Figure S4, the ET models illustrating the distribution and number of small vacuoles and medium vacuoles in GMC were distinct from those in Figure 2D, which was not observed in the other three stages. As an intermediate cell between meristemoid and YGC, GMC undergoes cell size growth, morphology transition, and symmetrical division, during which more nascent vacuoles may be required. Thus, this inherent variability might be due to the dynamic changes of vacuoles, in addition to the insufficient sample thickness. Future study with a time-lapse live-cell imaging on the Arabidopsis cotyledons (Han et al., 2018) could provide some answers underlying the inherent variability.

Membrane sources for vacuole biogenesis in stomatal lineage cells

As demonstrated by ET reconstruction in shoot apical meristem cells, nascent vacuoles were inherited from the mother cells during cytokinesis (Seguí-Simarro and Staehelin, 2006). However, the possibility of de novo vacuole biogenesis cannot be excluded during stomatal development. In a miniprotoplast system whose vacuoles were removed by centrifugation, lytic vacuoles regenerated 1 to 2 d after

evacuolation, thus demonstrating vacuole biogenesis in a well-differentiated plant cell (Yano et al., 2007). Our recent ET study also provided more convincing evidence for the de novo formation of MVBs-derived SVs and tubular vacuoles, both being shown to contribute to large central vacuole formation in the root meristem (Cui et al., 2019). In this study, vacuoles containing ILVs with various sizes have been identified in meristemoid and GMC (Figure 3, B and E), further confirming the role of small vacuoles in vacuole biogenesis during stomatal development. It is known that the pH value of the vacuolar lumen (about 5.2) is normally lower than that of MVB (about 6.2; Shen et al., 2013). The environmental pH change, which is transited from MVB to vacuole, may result in osmotic change, thus inducing the swelling of ILVs in the vacuoles. Consequently, swollen ILV bodies would gradually burst, which would contribute to the accumulation of vacuolar content, while it remains to be further investigated whether those small vacuoles without ILV originate from the fission of pre-existing large vacuoles (Figure 4C). Spherical membrane structures within the vacuolar lumen were also described before in the pavement cells on leaf epidermis, called "subvacuoles" (Hawes et al., 2001) or "bulbs" (Saito et al., 2002). The sizes of subvacuoles (ranging from 600 nm to 5,000 nm in diameter) were much larger than those of swollen ILVs (ranging from 50 nm to 200 nm in diameter). Their double-membrane characteristic and continuity with limiting vacuolar membranes were demonstrated by 3D reconstruction of serial thin sections (70 nm; Saito et al., 2002), suggesting that the subvacuoles are substantially distinct from the swollen ILVs identified in this study.

During the transition from meristemoid to GMC, the proportion of SVs constituting the total vacuolar volume increased dramatically, indicating the large formation of nascent SVs. Nevertheless, from YGC to GC, the inequivalence between the increase in total vacuolar volume and vacuole occupancy suggested that other cellular contents are replaced by vacuoles, accompanied by tonoplast and vacuole lumen expansion. In plants, LDs prominently serve as storage organelles providing lipids for membrane synthesis in addition to energy in metabolism (Huang et al., 2019). To investigate the role of LDs in vacuole formation during stomatal development, we therefore performed ET analysis on the LDs of the four cells (Supplemental Figure S8). An LD consists of a core of neutral lipids surrounded by a monolayer of phospholipids and LD-associated proteins (Huang et al., 2019), which shows transparent contents in TEM imaging (Figure 2, C, E, and G; Supplemental Figure S8, A, C, E, and G). The whole-cell ET models showed that LDs widely distributed along with the stomatal lineage cells from 3-dpg cotyledons (Supplemental Figure S8, B, D, F, and H). Further statistical analyses were also performed. Basically, we found that the LD parameters (e.g. amount, occupancy, and volume) were relatively higher in the YGC compared to those of the other three cell types (Supplemental Table S2). Notably, the combined LD volume of YGC was about three-fold of that of GC while the LD occupancy of YGC (3.78%) was almost seven-fold of that in GC (0.56%). Such a remarkable increment in YGC and decrease in GC of LD combined volume and cellular occupancy may indicate LD biogenesis in YGC and subsequent turnover in GC. It was reported that the LD abundance clearly decreased during light-induced stomatal opening, which is an active, energy-requiring process (McLachlan et al., 2016). The low LD volume in GC may be accompanied by LD metabolism for ATP production to support stomatal opening. Considering the vacuole volume and occupancy change in YGC and GC (Supplemental Table S1), the whole-cell ET models on LDs versus vacuoles may provide insights for the future studies on the possible role of LD biogenesis and turnover in vacuole formation and stomatal development.

In addition, other membranous organelles have also been shown to be involved in vacuole biogenesis, including trans-Golgi network (TGN), endoplasmic reticulum (ER), and autophagosome. TGN/TGN fusion was proposed to be responsible for the formation of the provacuole, a tubular structure which was thought to be a vacuole precursor (Marty, 1978). In addition, the freeze–etching technique enabled the identification of ER as the origin of vacuole biogenesis (Matile and Moor, 1968). The ER origin was supported by a recent study, where the provacuole was suggested to originate from ER thereby bypassing Golgi- or post-Golgi trafficking (Viotti et al., 2013). Autophagosome was also shown to be one of the membrane sources in vacuole biogenesis (Yano et al., 2007). Since the whole-cell ET technique enabled us to identify the role of MVB fusion and small vacuoles fusion/maturation in vacuole biogenesis during stomatal development, it will be feasible to explore the roles of other membranous organelles in relation with vacuole formation in the future. Moreover, it will be interesting to include stomatal development-deficient mutants (e.g. *mute*, *fama*, or *scrm1/ice1*; Ohashi-Ito and Bergmann, 2006; Pillitteri et al., 2007; Kanaoka et al., 2008) and stomatal function mutants (e.g. *ost1* or *slac1*; Mustilli et al., 2002; Vahisalu et al., 2008) in the ET analysis of vacuoles in future study.

Conclusions

In this study, we combined the whole-cell ET with CLSM approach to show the vacuole distribution and formation process in Arabidopsis stomatal lineage cells (Figure 6): (1) in the meristemoid, the single central large vacuole, which might be inherited from the MMC, contains swollen ILVs with size bigger than that of typical MVBs; (2) in the GMC, most of the vacuolar lumen contains swollen ILVs, albeit there are a small proportion of small vacuoles without ILV; (3) in the YGC, both convoluted and balloon-like large vacuoles were identified but no visible ILV were found inside these large vacuoles, and medium vacuoles may contribute to the central vacuole formation of mature GCs by fusing with large vacuoles; and (4) in the GC, the large vacuoles were either simultaneously interconnected or separated in both GCs of the same stomatal pair.

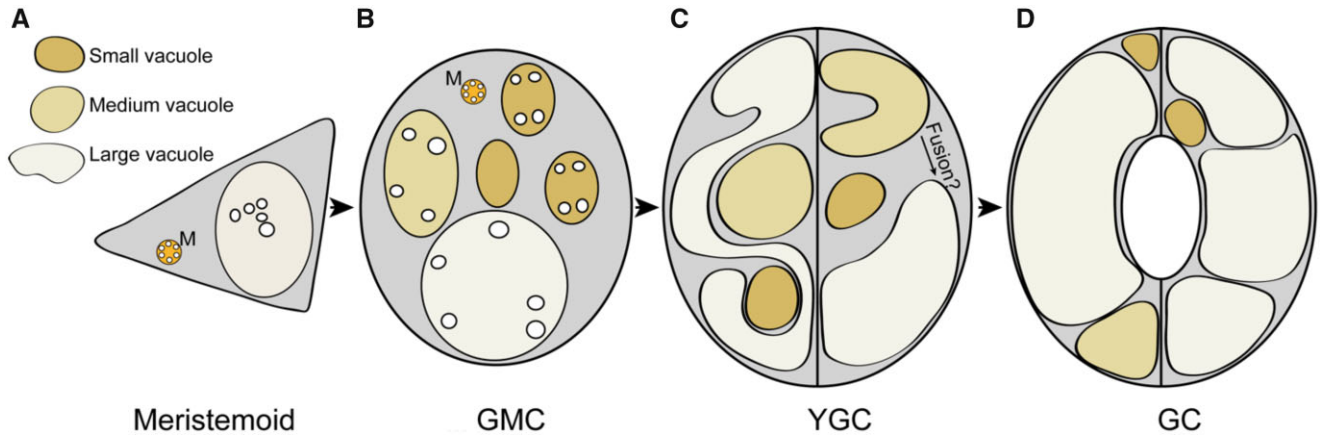

Figure 6 Working model of vacuole formation and distribution in Arabidopsis stomatal lineage cells. Distribution and morphology of vacuoles are based on the whole-cell ET analysis of individual stomatal lineage cells in this study, including meristemoid (A), GMC (B), YGC (C), and GC (D). ET, electron tomography; M, multivesicular body.

The working model is based on whole-cell ET analysis of individual stomatal lineage cells. However, several questions can be asked in the future study, e.g. where did the pre-existing large vacuole of the meristemoid come from? What is the relationship between the large vacuoles in the meristemoid and GMC? Is the large vacuole in the GMC inherited from that in the meristemoid or derived from de novo formation and fusion of vacuoles? Some of them can be addressed using a combination of live-cell imaging (Komis et al., 2015; Ito et al., 2018; Liu et al., 2021b) with correlative light-electron microscopy (CLEM) or ET (Hoffman et al., 2020) to illustrate the dynamics of vacuole formation and correlate the dynamic changes with corresponding structures at the nanometer resolution via CLEM/ET analysis.

Materials and methods

Plant materials and growth conditions

The Arabidopsis (*A. thaliana*) wild-type and transgenic plants expressing YFP-VAMP711 or Aleu-Kaede were in Columbia background. Transgenic Arabidopsis plants expressing Aleu-Kaede were generated as previously described (Cui et al., 2019). Transgenic Arabidopsis plants expressing YFP-VAMP711 (WAVE_9Y) were obtained from the Nottingham Arabidopsis Stock Center (Geldner et al., 2009).

Arabidopsis seeds were surface sterilized by 70% [v/v] ethanol and grown on plates with half-strength Murashige and Skoog (MS) growth medium (pH 5.7) supplemented by 1% [w/v] sucrose and 0.8% [w/v] agar. Seeds were stratified at 4°C for 2 d before being transferred to the growth chamber (white fluorescent light bulb 120 μE m^{-2} s^{-1}) at 22°C under a long day (16-h light/8-h dark) photoperiod.

Chemicals

All chemicals were dissolved in DMSO and were applied in liquid half-strength MS medium before imaging. The detached leaves were submerged in PI (10 μg·mL^{-1}), followed by rinsing in water to remove excess staining and then imaging immediately. The staining of FM4–64 is modified from previous method (Scheuring et al., 2015). The detached leaves were proceeded for overnight incubation of FM4–64 (4 μM) and constant washing in half-strength MS for 5 h in orbital shaker before imaging. PI and FM4–64 were obtained from Sigma-Aldrich and Life Technologies, respectively.

Confocal microscopy and photoconversion assay

Confocal imaging was performed using Leica SP8 CLSM with 63× objective, NA 1.30 (Leica Microsystems, Germany). GFP was excited using 488-nm laser (1% intensity), 505–550 nm emission range and the standard mode of the HyD detector (gain = 400). RFP was excited using 561-nm laser (1% intensity), 590–650 nm emission range and the standard mode of the HyD detector (gain = 100). Pinhole was set to 1AU, scanning speed was set to 400 Hz, line average to 3, pixel resolution was set to 1024 × 1024. For z-stack imaging, step size was set to 0.4 μm and number of optical slices was system optimized.

For surface rendering reconstruction of vacuoles, Imaris 9.6.0 (Bitplane) was used. For each cell, cell walls of the DIC (differential interference contrast) channel were used to create a masked channel, in which signal intensity for the voxels outside were set to 0. The newly built channel was used to create surface models of vacuoles and nuclei automatically. The surfaces detail was set to 0.15 μm. The obtained model was manual adjusted with threshold option to match with background fluorescent signals.

Photoconversion experiments were performed in the FRAP module of SP8 confocal microscope as described previously (Sattarzadeh et al., 2015). In order to block vacuolar degradation activity prior to photoconversion, detached Arabidopsis leaves expressing Aleu-Kaede were submerged in MS medium containing 0.5-μM concanamycin A for 8 h. Photoconversion was performed using 405-nm laser at 75% laser power twice for each trial. Green fluorescence was detected with a spectral detector between 505 and 550 nm

(gain = 100) and red fluorescence was detected with a spectral detector between 590 and 630 nm (gain = 100).

High-pressure freezing and freeze substitution

The general procedures for high-pressure freezing and freeze substitution were performed essentially as described previously (Kang, 2010). Briefly, 3-dpg Arabidopsis cotyledons were dissected and rapidly frozen in HPM100 high-pressure freezer (Leica Microsystems, Germany). For ultrastructural analysis, the subsequent freeze substitution was performed at −80°C for 72 h in 2% osmium tetroxide (OsO_4) dissolved in anhydrous acetone and excess OsO_4 was removed by rinsing with precooled acetone. After gradually warmed to −20°C over a 24-h period, the samples were incubated at −20°C for 12 h and then gradual warmed to 4°C over a 4-h period. Tissue samples were removed from planchettes and slowly infiltrated stepwise with increasing concentrations of Embed-812 resin (catalog no. 14120; Electron Microscopy Sciences, USA) over 96 h. The sample polymerization was performed at 60°C for 48 h. The blocks were trimmed and sectioned using a diamond knife (Diatome, Switzerland) and an UC7 ultramicrotome (Leica Microsystems, Germany). Serial sections were collected onto formvar-coated copper slot grids (catalog no. GS2010-Cu; Electron Microscopy Sciences, USA), followed by a post-staining procedure using 2% uranyl acetate (w/v, 70% methanol) and Reynold's lead citrate (Reynolds, 1963). Before ET, sections were examined using a Hitachi H-7650 transmission electron microscope with a charge-coupled device camera operating at 80 kV (Hitachi High-Technologies, Japan).

Electron tomography

The general procedures to perform ET have been described previously (Toyooka and Kang, 2014). In brief, 250-nm-thick sections were recorded using a Tecnai F20 electron microscope (Thermo Fisher Scientific, USA) operated at 200 kV. For each grid, a tilt image stack (81 images) from +60° to −60° with 1.5° intervals was collected and the second tilt image stack was collected by rotating the grid with 90°. Dual-axis tomograms were calculated from pairs of image stacks with the etomo program of the IMOD software package (version 4.9.13). The 15-nm gold particles (BBI Solutions, UK) at both surfaces of sections were used as fiducial markers to align individual images in the tilt series. After ET analysis, the IMOD software can display an optical slice cut through the 3D image data in any chosen orientation. The magnifications were 6,500× (Figure 2A), 5,000× (Supplemental Figure S6), 3,500× (Figure 2, C and E; Supplemental Figures S4 and S5), and 2,500× (Figure 2G), corresponding to a pixel size of 3.38 nm, 4.32 nm, 6.31 nm, and 8.66 nm, respectively. For model generation, the contours were drawn and meshed with the 3dmod program in the IMOD software package. To compensate for thinning of plastic sections during electron imaging, "Z-scale" factors were adjusted in the 3dmod interface. The scaling factors were determined using spherical MVBs as described previously (Kang, 2010). In this study, we used round MVBs in tomograms to determine their z-scale factors. First, the radius of an MVB was measured in the xy tomographic slice, and the z-scale factor was set to make the MVB radius equal in the yz slice. The factors were calculated to be approximately 1.3 for meristemoid and 1.0 for other tomograms.

Quantification and statistical analysis

All detailed statistical details parameters of the experiments can be found in the figure legends. The volume and surface area of individual vacuole were generated and obtained from the IMOD software. The score of volume–surface ratio was determined by dividing vacuole volume (nm^3) by surface area (nm^2). Statistical analyses were performed using GraphPad Prism version 8.0 (GraphPad Software).

Accession numbers

Gene sequence data in this article can be found in the Arabidopsis Information Resource (TAIR) database: VAMP711 (AT4G32150).

Supplemental data

The following materials are available in the online version of this article.

Supplemental Figure S1. Overview of leaf epidermis in the two transgenic Arabidopsis marker lines.

Supplemental Figure S2. Multiple examples of stomatal lineage cells in transgenic plants expressing the tonoplast marker YFP-VAMP711.

Supplemental Figure S3. Multiple examples of the four stomatal lineage cells used for 3D ET analysis and model reconstruction.

Supplemental Figure S4. ET analysis of vacuoles on other candidates of the four stomatal lineage cells.

Supplemental Figure S5. ET analysis of vacuoles on closed stomata of Arabidopsis cotyledon epidermis.

Supplemental Figure S6. The large vacuole split into two parts separated by newly formed cell wall in a GMC during cytokinesis.

Supplemental Figure S7. Distributions of the tonoplast in open and closed stomata.

Supplemental Figure S8. Whole-cell ET analyses of LDs in stomatal lineage cells of Arabidopsis cotyledon epidermis.

Supplemental Table S1. Quantification analyses of vacuolar parameters in the four developmental stages of stomatal lineage cells.

Supplemental Table S2. Quantification analyses of LD parameters in the four developmental stages of stomatal lineage cells.

Supplemental Movie S1. The whole-cell ET reconstruction of vacuoles in meristemoid.

Supplemental Movie S2. The whole-cell ET reconstruction of vacuoles in GMC.

Supplemental Movie S3. The whole-cell ET reconstruction of vacuoles in YGC.

Supplemental Movie S4. The whole-cell ET reconstruction of vacuoles in GC.

Supplemental Movie S5. The ET reconstructions of vacuoles in three closed stomata.

Supplemental Movie S6. The ET reconstruction of vacuoles in the symmetrically dividing GMC.

Supplemental Movie S7. The ET model displaying vacuoles containing swollen ILVs in GMC.

Supplemental Movie S8. The ET reconstruction of a MVB from WT Arabidopsis cotyledon epidermis.

Acknowledgments

We would like to thank Dr Dominique Bergmann (Stanford University) for providing us the transgenic Arabidopsis lines MUTEp::GFP-NLS and FAMAp::GFP-FAMA.

Funding

This work was supported by grants from the National Natural Science Foundation of China (91854201), the Research Grants Council of Hong Kong (AoE/M-05/12, CUHK 14102417, 14100818, 14101219, C4033-19E, C4002-17G, C4002-20W, C2009-19G, G-CUHK410/19 and R4005-18), and The Chinese University of Hong Kong (CUHK) Research Committee and CAS-Croucher Funding Scheme for Joint Laboratories to L.J.

Conflict of interest statement. The authors declare that there is no conflict of interest.

References

Adell MAY, Vogel GF, Pakdel M, Müller M, Lindner H, Hess MW, Teis D (2014) Coordinated binding of Vps4 to ESCRT-III drives membrane neck constriction during MVB vesicle formation. J Cell Biol **205:** 33–49

Adrian J, Chang J, Ballenger CE, Bargmann BO, Alassimone J, Davies KA, Lau OS, Matos JL, Hachez C, Lanctot A, et al. (2015) Transcriptome dynamics of the stomatal lineage: birth, amplification, and termination of a self-renewing population. Dev Cell **33:** 107–118

Andrés Z, Pérez-Hormaeche J, Leidi EO, Schlücking K, Steinhorst L, McLachlan DH, Schumacher K, Hetherington AM, Kudla J, Cubero B, Pardo JM (2014) Control of vacuolar dynamics and regulation of stomatal aperture by tonoplast potassium uptake. Proc Natl Acad Sci USA **111:** E1806–E1814

Bak G, Lee E-J, Lee Y, Kato M, Segami S, Sze H, Maeshima M, Hwang J-U, Lee Y (2013) Rapid structural changes and acidification of guard cell vacuoles during stomatal closure require phosphatidylinositol 3,5-bisphosphate. Plant Cell **25:** 2202–2216

Bergmann DC, Sack FD (2007) Stomatal development. Annu Rev Plant Biol **58:** 163–181

Brown RC, Lemmon BE (1985) Development of stomata in selaginella: division polarity and plastid movements. Am J Bot **72:** 1914–1925

Buono RA, Leier A, Paez-Valencia J, Pennington J, Goodman K, Miller N, Ahlquist P, Marquez-Lago TT, Otegui MS (2017) ESCRT-mediated vesicle concatenation in plant endosomes. J Cell Biol **216:** 2167–2177

Cui Y, Cao W, He Y, Zhao Q, Wakazaki M, Zhuang X, Gao J, Zeng Y, Gao C, Ding Y, et al. (2019) A whole-cell electron tomography model of vacuole biogenesis in *Arabidopsis* root cells. Nat Plant **5:** 95–105

Cui Y, Zhao Q, Gao C, Ding Y, Zeng Y, Ueda T, Nakano A, Jiang L (2014) Activation of the Rab7 GTPase by the MON1-CCZ1 complex is essential for PVC-to-vacuole trafficking and plant growth in *Arabidopsis*. Plant Cell **26:** 2080–2097

Cui Y, Zhao Q, Hu S, Jiang L (2020) Vacuole biogenesis in plants: how many vacuoles, how many models? Trends Plant Sci **25:** 538–548

Dong J, MacAlister CA, Bergmann DC (2009) BASL controls asymmetric cell division in *Arabidopsis*. Cell **137:** 1320–1330

Fricker MD (1990) Volume measurement of guard cell vacuoles during stomatal movements using confocal microscopy. Trans R Microsc Soc **1:** 345–348

Gao C, Luo M, Zhao Q, Yang R, Cui Y, Zeng Y, Xia J, Jiang L (2014) A unique plant ESCRT component, FREE1, regulates multivesicular body protein sorting and plant growth. Curr Biol **24:** 2556–2563

Gao X, Li C, Wei P, Zhang X, Chen J, Wang X (2005) The dynamic changes of tonoplasts in guard cells are important for stomatal movement in *Vicia faba*. Plant Physiol **139:** 1207–1216

Gao X, Wang X, Ren F, Chen J, Wang X (2009) Dynamics of vacuoles and actin filaments in guard cells and their roles in stomatal movement. Plant Cell Environ **32:** 1108–1116

Geisler M, Nadeau J, Sack FD (2000) Oriented asymmetric divisions that generate the stomatal spacing pattern in arabidopsis are disrupted by the *too many mouths* mutation. Plant Cell **12:** 2075–2086

Geldner N, Denervaud-Tendon V, Hyman DL, Mayer U, Stierhof YD, Chory J (2009) Rapid, combinatorial analysis of membrane compartments in intact plants with a multicolor marker set. Plant J **59:** 169–178

Gudesblat GE, Torres PS, Vojnov AA (2009) Stomata and pathogens: warfare at the gates. Plant Signal Behav **4:** 1114–1116

Han S-K, Qi X, Sugihara K, Dang JH, Endo TA, Miller KL, Kim E-D, Miura T, Torii KU (2018) MUTE directly orchestrates cell-state switch and the single symmetric division to create stomata. Dev Cell **45:** 303–315.e305

Hawes C, Saint-Jore CM, Brandizzi F, Zheng H, Andreeva AV, Boevink P (2001) Cytoplasmic illuminations: in planta targeting of fluorescent proteins to cellular organelles. Protoplasma **215:** 77–88

Hetherington AM, Woodward FI (2003) The role of stomata in sensing and driving environmental change. Nature **424:** 901–908

Hoffman DP, Shtengel G, Xu CS, Campbell KR, Freeman M, Wang L, Milkie DE, Pasolli HA, Iyer N, Bogovic JA, et al. (2020) Correlative three-dimensional super-resolution and block-face electron microscopy of whole vitreously frozen cells. Science **367**: eaaz5357

Hosotani S, Yamauchi S, Kobayashi H, Fuji S, Koya S, Shimazaki K-i, Takemiya A (2021) A BLUS1 kinase signal and a decrease in intercellular CO_2 concentration are necessary for stomatal opening in response to blue light. Plant Cell **33:** 1813–1827

Hsu P-K, Dubeaux G, Takahashi Y, Schroeder JI (2021) Signaling mechanisms in abscisic acid-mediated stomatal closure. Plant J **105:** 307–321

Huang S, Jiang L, Zhuang X (2019) Possible roles of membrane trafficking components for lipid droplet dynamics in higher plants and green algae. Front Plant Sci **10**:207

Huang S, Waadt R, Nuhkat M, Kollist H, Hedrich R, Roelfsema MRG (2019) Calcium signals in guard cells enhance the efficiency by which abscisic acid triggers stomatal closure. New Phytol **224:** 177–187

Hunter PR, Craddock CP, Di Benedetto S, Roberts LM, Frigerio L (2007) Fluorescent reporter proteins for the tonoplast and the vacuolar lumen identify a single vacuolar compartment in *Arabidopsis* cells. Plant Physiol **145:** 1371–1382

Inoue S-i, Kinoshita T (2017) Blue light regulation of stomatal opening and the plasma membrane H^+-ATPase. Plant Physiol **174:** 531–538

Ito Y, Uemura T, Nakano A (2018) The Golgi entry core compartment functions as a COPII-independent scaffold for ER-to-Golgi transport in plant cells. J Cell Sci **131**: jcs203893

Jahn R, Lang T, Sudhof TC (2003) Membrane fusion. Cell **112:** 519–533

Jauh G-Y, Phillips TE, Rogers JC (1999) Tonoplast intrinsic protein isoforms as markers for vacuolar functions. Plant Cell **11:** 1867–1882

Kanaoka MM, Pillitteri LJ, Fujii H, Yoshida Y, Bogenschutz NL, Takabayashi J, Zhu J-K, Torii KU (2008) SCREAM/ICE1 and SCREAM2 specify three cell-state transitional steps leading to Arabidopsis stomatal differentiation. Plant Cell **20:** 1775–1785

Kang B-H (2010) Chapter 12-Electron microscopy and high-pressure freezing of *Arabidopsis*. In T Müller-Reichert, ed, Methods in Cell Biology, Vol **96**. Academic Press, Cambridge, MA, pp 259–283

Kim DJ, Lee JS (2007) Current theories for mechanism of stomatal opening: influence of blue light; mesophyll cells, and sucrose. J Plant Biol **50:** 523–526

Kim T-H, Böhmer M, Hu H, Nishimura N, Schroeder JI (2010) Guard cell signal transduction network: advances in understanding abscisic acid, CO_2, and Ca^{2+} signaling. Annu Rev Plant Biol **61:** 561–591

Kolb C, Nagel M-K, Kalinowska K, Hagmann J, Ichikawa M, Anzenberger F, Alkofer A, Sato MH, Braun P, Isono E (2015) FYVE1 is essential for vacuole biogenesis and intracellular trafficking in Arabidopsis. Plant Physiol **167:** 1361–1373

Komis G, Mistrik M, Šamajová O, Ovečka M, Bartek J, Šamaj J (2015) Superresolution live imaging of plant cells using structured illumination microscopy. Nat Protoc **10:** 1248–1263

Larkin JC, Marks MD, Nadeau J, Sack F (1997) Epidermal cell fate and patterning in leaves. Plant Cell **9:** 1109–1120

Larkin JC, Young N, Prigge M, Marks MD (1996) The control of trichome spacing and number in *Arabidopsis*. Development **122:** 997–1005

Liu C, Zeng Y, Li H, Yang C, Shen W, Xu M, Xiao Z, Chen T, Li B, Cao W, et al. (2021a) A plant unique ESCRT component, FYVE4, regulates multivesicular endosome biogenesis and plant growth. New Phytol **231:** 193–209

Liu Z, Gao J, Cui Y, Klumpe S, Xiang Y, Erdmann PS, Jiang L (2021b) Membrane imaging in the plant endomembrane system. Plant Physiol **185:** 562–576

Marty F (1978) Cytochemical studies on GERL, provacuoles, and vacuoles in root meristematic cells of *Euphorbia*. Proc Natl Acad Sci USA **75:** 852–856

Marty F (1999) Plant vacuoles. Plant Cell **11:** 587–599

Matile PH, Moor H (1968) Vacuolation: origin and development of the lysosomal apparatus in root-tip cells. Planta **80:** 159–175

Matsuoka K, Higuchi T, Maeshima M, Nakamura K (1997) A vacuolar-type H^+-ATPase in a nonvacuolar organelle is required for the sorting of soluble vacuolar protein precursors in tobacco cells. Plant Cell **9:** 533–546

McLachlan Deirdre H, Lan J, Geilfus C-M, Dodd Antony N, Larson T, Baker A, Hõrak H, Kollist H, He Z, Graham I, et al. (2016) The breakdown of stored triacylglycerols is required during light-induced stomatal opening. Curr Biol **26:** 707–712

Meckel T, Gall L, Semrau S, Homann U, Thiel G (2007) Guard cells elongate: relationship of volume and surface area during stomatal movement. Biophys J **92:** 1072–1080

Meyer S, Scholz-Starke J, Angeli AD, Kovermann P, Burla B, Gambale F, Martinoia E (2011) Malate transport by the vacuolar *At*ALMT6 channel in guard cells is subject to multiple regulation. Plant J **67:** 247–257

Munemasa S, Hauser F, Park J, Waadt R, Brandt B, Schroeder JI (2015) Mechanisms of abscisic acid-mediated control of stomatal aperture. Curr Opin Plant Biol **28:** 154–162

Murk JLAN, Humbel BM, Ziese U, Griffith JM, Posthuma G, Slot JW, Koster AJ, Verkleij AJ, Geuze HJ, Kleijmeer MJ (2003) Endosomal compartmentalization in three dimensions: Implications for membrane fusion. Proc Natl Acad Sci USA **100:** 13332–13337

Mustilli AC, Merlot S, Vavasseur A, Fenzi F, Giraudat J (2002) *Arabidopsis* OST1 protein kinase mediates the regulation of stomatal aperture by abscisic acid and acts upstream of reactive oxygen species production. Plant Cell **14:** 3089–3099

Ohashi-Ito K, Bergmann DC (2006) Arabidopsis FAMA controls the final proliferation/differentiation switch during stomatal development. Plant Cell **18:** 2493–2505

Olbrich A, Hillmer S, Hinz G, Oliviusson P, Robinson DG (2007) Newly formed vacuoles in root meristems of barley and pea seedlings have characteristics of both protein storage and lytic vacuoles. Plant Physiol **145:** 1383–1394

Otegui MS, Herder R, Schulze J, Jung R, Staehelin LA (2006) The proteolytic processing of seed storage proteins in *Arabidopsis* embryo cells starts in the multivesicular bodies. Plant Cell **18:** 2567–2581

Pandey S, Zhang W, Assmann SM (2007) Roles of ion channels and transporters in guard cell signal transduction. FEBS Lett **581:** 2325–2336

Paris N, Stanley CM, Jones RL, Rogers JC (1996) Plant cells contain two functionally distinct vacuolar compartments. Cell **85:** 563–572

Pillitteri LJ, Peterson KM, Horst RJ, Torii KU (2011) Molecular profiling of stomatal meristemoids reveals new component of asymmetric cell division and commonalities among stem cell populations in *Arabidopsis*. Plant Cell **23:** 3260–3275

Pillitteri LJ, Sloan DB, Bogenschutz NL, Torii KU (2007) Termination of asymmetric cell division and differentiation of stomata. Nature **445:** 501–505

Pillitteri LJ, Torii KU (2012) Mechanisms of stomatal development. Annu Rev Plant Biol **63:** 591–614

Reynolds ES (1963) The use of lead citrate at high pH as an electron-opaque stain in electron microscopy. J Cell Biol **17:** 208–212

Rojo E, Gillmor CS, Kovaleva V, Somerville CR, Raikhel NV (2001) VACUOLELESS1 is an essential gene required for vacuole formation and morphogenesis in *Arabidopsis*. Dev Cell **1:** 303–310

Saito C, Ueda T, Abe H, Wada Y, Kuroiwa T, Hisada A, Furuya M, Nakano A (2002) A complex and mobile structure forms a distinct subregion within the continuous vacuolar membrane in young cotyledons of *Arabidopsis*. Plant J **29:** 245–255

Sattarzadeh A, Saberianfar R, Zipfel WR, Menassa R, Hanson MR (2015) Green to red photoconversion of GFP for protein tracking *in vivo*. Scient Rep **5:** 11771

Scarth GW (1927) Stomatal movement: Its regulation and regulatory role a review. Protoplasma **2:** 498–511

Scheuring D, Löfke C, Krüger F, Kittelmann M, Eisa A, Hughes L, Smith RS, Hawes C, Schumacher K, Kleine-Vehn J (2016) Actin-dependent vacuolar occupancy of the cell determines auxin-induced growth repression. Proc Natl Acad Sci USA **113:** 452–457

Scheuring D, Schöller M, Kleine-Vehn J, Löfke C (2015) Vacuolar staining methods in plant cells. Methods Mol Biol **1242:** 83–92

Schroeder JI, Allen GJ, Hugouvieux V, Kwak JM, Waner D (2001) Guard cell signal transduction. Annu Rev Plant Physiol Plant Mol Biol **52:** 627–658

Seguí-Simarro JM, Staehelin LA (2006) Cell cycle-dependent changes in Golgi stacks, vacuoles, clathrin-coated vesicles and multivesicular bodies in meristematic cells of *Arabidopsis thaliana*: a quantitative and spatial analysis. Planta **223:** 223–236

Shen J, Zeng Y, Zhuang X, Sun L, Yao X, Pimpl P, Jiang L (2013) Organelle pH in the *Arabidopsis* endomembrane system. Mol Plant **6:** 1419–1437

Shen J, Zhao Q, Wang X, Gao C, Zhu Y, Zeng Y, Jiang L (2018) A plant Bro1 domain protein BRAF regulates multivesicular body biogenesis and membrane protein homeostasis. Nat Commun **9:** 3784

Shimada T, Takagi J, Ichino T, Shirakawa M, Hara-Nishimura I (2018) Plant vacuoles. Annu Rev Plant Biol **69:** 123–145

Shope JC, DeWald DB, Mott KA (2003) Changes in surface area of intact guard cells are correlated with membrane internalization. Plant Physiol **133:** 1314–1321

Tanaka Y, Kutsuna N, Kanazawa Y, Kondo N, Hasezawa S, Sano T (2007) Intra-vacuolar reserves of membranes during stomatal closure: the possible role of guard cell vacuoles estimated by 3-D reconstruction. Plant Cell Physiol **48:** 1159–1169

Toyooka K, Kang B-H (2014) Reconstructing plant cells in 3D by serial section electron tomography. *In* V Žárský, F Cvrčková, eds, Plant Cell Morphogenesis. Springer, New York, pp 159–170

Uemura T, Yoshimura SH, Takeyasu K, Sato MH (2002) Vacuolar membrane dynamics revealed by GFP-*At*Vam3 fusion protein. Genes Cells **7:** 743–753

Vahisalu T, Kollist H, Wang YF, Nishimura N, Chan WY, Valerio G, Lamminmäki A, Brosché M, Moldau H, Desikan R, et al. (2008) SLAC1 is required for plant guard cell S-type anion channel function in stomatal signalling. Nature **452:** 487–491

Viotti C, Krüger F, Krebs M, Neubert C, Fink F, Lupanga U, Scheuring D, Boutté Y, Frescatada-Rosa M, Wolfenstetter S, et al. (2013) The endoplasmic reticulum is the main membrane source for biogenesis of the lytic vacuole in *Arabidopsis*. Plant Cell **25:** 3434–3449

Weiner E, Pinskey JM, Nicastro D, Otegui MS (2022) Electron microscopy for imaging organelles in plants and algae. Plant Physiol **188:** 713–725

Yano K, Hattori M, Moriyasu Y (2007) A novel type of autophagy occurs together with vacuole genesis in miniprotoplasts prepared from tobacco culture cells. Autophagy **3:** 215–221

Zhao L, Sack FD (1999) Ultrastructure of stomatal development in *Arabidopsis* (*Brassicaceae*) leaves. Am J Bot **86:** 929–939

Zheng H, Staehelin LA (2011) Protein storage vacuoles are transformed into lytic vacuoles in root meristematic cells of germinating seedlings by multiple, cell type-specific mechanisms. Plant Physiol **155:** 2023–2035